J. Space Weather Space Clim. 2026, **16**, 18

https://doi.org/10.1051/swsc/2026007

JSWSC

Available online at:
www.swsc-journal.org

RESEARCH ARTICLE OPEN ACCESS

Field-aligned currents are strongly modulated by corotating solar wind high-speed streams

Rajkumar Hajra[1], Bruce T. Tsurutani[2], Adriane M. S. Franco[3,4,a], Quanming Lu[1], Aimin Du[5], Gurbax S. Lakhina[6], San Lu[1], Xinliang Gao[1], and Ezequiel Echer[7]

[1] CAS Key Laboratory of Geospace Environment, School of Earth and Space Sciences, University of Science and Technology of China, Hefei, PR China
[2] Retired, Pasadena, California, USA
[3] Federal University of Southern and Southeastern Pará, Marabá, Brazil
[4] Federal University of Jataí (UFJ), Jataí, Brazil
[5] College of Earth and Planetary Sciences, Chinese Academy of Sciences, Beijing, PR China
[6] Retired, Navi Mumbai, India
[7] Instituto Nacional de Pesquisas Espaciais, São José dos Campos, São Paulo, Brazil

Received 3 November 2025 / Accepted 27 February 2026

Abstract – Birkeland field-aligned currents (FACs) are associated with solar wind-magnetosphere energy coupling leading to substorms/convection events. FAC intensity enhancements have been studied during geomagnetic storms driven by interplanetary coronal mass ejections and corotating interaction regions. Here we present an in-depth analysis of long-term FAC variation, strongly modulated by solar wind high-speed streams (HSSs) emanated from solar coronal holes. Variations of both dayside and nightside FAC intensities during June 2016 through June 2017 are characterized by prominent periodicities of ∼14, ∼26, and ∼29 days (in descending order of amplitude), highly correlated to the empirically estimated rate of magnetic flux opening at the dayside magnetopause. The periodicities represent the ∼27-day solar rotation period and its harmonic, resulting from the combined impacts of recurring HSSs emanated from multiple long-lived coronal holes, corotating with the Sun. Modulation of the long-term FAC intensity variation by recurring HSSs is confirmed by statistical regression, cross-wavelet, and coherence analyses. These results may be useful in developing FAC prediction models.

Keywords: Field-aligned current / High-speed streams / Coronal holes / Interplanetary magnetic field / Solar rotation

1 Introduction

The Birkeland geomagnetic field-aligned currents (FACs; Birkeland, 1908) are an important aspect of the solar wind-magnetosphere-ionosphere coupling. The two-component currents consist of a poleward region 1 component closing via the dayside magnetopause, and an equatorward region 2 component closing in the nightside partial ring current (Iijima & Potemra, 1976, 1978). Thus, they are closely related to magnetic reconnection (Dungey, 1961) and/or viscous interaction (Axford & Hines, 1961) at the magnetopause and substorm activity. See also Tsurutani et al. (1998, 2001) and Lakhina et al. (2000, 2003) for plasma waves in the polar cap boundary layer. During the last few decades, significant progress has been made on understanding the origin of FACs and their dependence on ionospheric conductivity, seasons, geomagnetic storms, and substorms. Dayside FAC intensities are known to exhibit an annual variation with a summer peak and a winter minimum, the summer FAC intensity being ∼2 times the winter FAC intensity on average (Fujii et al., 1981; Wang et al., 2005; Coxon et al., 2016; Hajra et al., 2025c). Based on a statistical study of FACs during 2900 substorms, Coxon et al. (2014a) reported a prominent increase in the FAC magnitude in the substorm growth phase, peaking in the expansion phase, followed by a decrease to pre-substorm level in the substorm recovery phase. The maximum increase of the FAC magnitude (intensity) was found to be ∼1 MA during a substorm cycle. The substorm-related current magnitudes were found (Coxon et al., 2014b) to be strongly related to empirically-estimated magnetic reconnection rate Φ_D at the dayside magnetopause (Milan et al., 2012). For geomagnetic storms driven by corotating interaction regions (CIRs) and interplanetary coronal mass ejections

[a]The affiliation of this author changed during the publication process.
*Corresponding author: rhajra@ustc.edu.cn, rajkumarhajra@yahoo.co.in

(ICMEs), FAC magnitudes have been reported to maximize at ~40 min and ~1 h, respectively, after the storm onset (Pedersen et al., 2021, 2022). Pedersen et al. (2023) reported a delayed response of FACs from the Newell coupling function $N_{CF,}$ which provides an empirical measure of the rate at which magnetopause magnetic fluxes are opened (Newell et al., 2007). Total time-integrated FAC intensities were found to lag behind N_{CF} by ~40 min during storms driven by CIRs and interplanetary sheaths. The delay was ~1 h for storms driven by magnetic clouds (MCs). FAC intensifications up to a factor of ~10 have been reported during strong geomagnetic storms, compared to the quiet time FAC intensities (Wang et al., 2006, 2024; Wilder et al., 2012; Knipp et al., 2014; Le et al., 2016; Lyons et al., 2016; Pedersen et al., 2022; Hajra et al., 2024a, 2024b). Recent studies show that high-intensity long-duration continuous auroral electrojet (AE) activities (HILDCAAs; Tsurutani & Gonzalez, 1987), which are caused by interplanetary Alfvén waves primarily during the solar cycle declining phase (Hajra et al., 2013), may lead to sustained FAC intensity enhancements by a factor of ~5 for several days (Hajra et al., 2025a, 2025b).

The purpose of this work is to study the modulation of the long-term FAC variations by solar wind high-speed streams (HSSs) emanated from solar coronal holes. It is well known that HSSs modulate the magnetosphere-ionosphere system, leading to outer radiation belt relativistic electron flux enhancements (Paulikas & Blake, 1979; Hajra et al., 2014a, 2015a, 2015b, 2024c; Tsurutani et al., 2016; Hajra & Tsurutani, 2018; Hajra 2021), recurrence of moderate intensity geomagnetic storms (Tsurutani et al., 1995, 2006b; Alves et al., 2006; Chi et al., 2018), intensification of substorms and associated ionospheric energy dissipation (e.g., Tanskanen et al., 2005), and occurrences of HILDCAAs (Tsurutani & Gonzalez, 1987; Hajra et al., 2013, 2014b). While variability of FACs during storms, substorms, and HILDCAAs, and dependences of FACs on solar wind coupling have been extensively studied, the influence of HSSs on the long-term FAC variations has not been explored in detail. In the present work, we will study FAC intensity variations from June 2016 through June 2017, during the minimum phase between solar cycles 24 and 25. During this ~1-year interval, the terrestrial magnetosphere encountered a series of HSSs emanating from solar coronal holes.

2 Data and methods

2.1 The FAC database

The radial FAC intensity data analyzed in this work are based on magnetic field measurements by ~70 polar Iridium® satellites of the Active Magnetosphere and Planetary Electrodynamics Response Experiment (AMPERE; Waters et al., 2001; Anderson et al., 2002). The FAC intensity time series (at a resolution of 2 min) from 1 June 2016 through 30 June 2017 is obtained from the AMPERE Science Data Center of the Johns Hopkins Physics Laboratory. We estimated total northern and southern hemispheric FAC intensities FAC_T using FAC intensity upward (FAC_{up}) and downward (FAC_{down}) components: $FAC_T = 1/2\ (FAC_{up} - FAC_{down})$. Given that FAC_{up} and FAC_{down} are positive and negative quantities, respectively, FAC_T is defined as a positive quantity. We have considered dayside and nightside currents separately as well, where they refer to 06–18 magnetic local time (MLT) and 18–06 MLT, respectively, in altitude-adjusted corrected geomagnetic coordinate (AACGM; Baker & Wing, 1989) local time.

2.2 The solar wind measurements

Upstream solar wind plasma and interplanetary magnetic field (IMF) measurements (1-min resolution) are obtained from NASA's OMNIWeb Plus database (King & Papitashvili, 2020). The IMF vector components are in the geocentric solar magnetospheric (GSM) coordinate system. This system has the x-axis directed toward the sun, and the *y*-axis is in the $\boldsymbol{\Omega} \times \hat{\boldsymbol{x}}/|\boldsymbol{\Omega} \times \hat{\boldsymbol{x}}|$-direction, where $\boldsymbol{\Omega}$ is the magnetic dipole pole in the northern hemisphere. The z-axis completes a right-hand system.

2.3 Identifications of HSSs and CIRs

From the solar wind proton speed V_p temporal variation, an HSS is identified with a peak $V_p \gtrsim 500\ \mathrm{km\ s^{-1}}$, preceded by a gradual rise and followed by a slower decay (Tsurutani et al., 1995). Origin of the HSS from a solar coronal hole (Krieger et al., 1973) is confirmed by analysis of solar coronal images taken by the Atmospheric Imaging Assembly (AIA) onboard NASA's Solar Dynamic Observatory (SDO) and the solar synoptic maps obtained from the Space Weather Prediction Center of the National Oceanic and Atmospheric Administration (NOAA). Enhanced proton density N_p, ram pressure P_{sw}, and IMF magnitude B_0 in the interaction region between the HSS and a slow solar wind are signatures of a CIR (Smith & Wolfe, 1976).

2.4 Estimation of coupling functions

Using in-situ solar wind measurements, we estimated the Newell coupling function N_{CF} and the Φ_D parameter. N_{CF}, computed as $V_p^{4/3} B_{yz}^{2/3} \sin^{8/3}(\theta/2)$, gives an empirical estimate of the rate at which magnetic fluxes are opened at the magnetopause (Newell et al., 2007). Φ_D presents the rate of dayside magnetopause reconnection, empirically estimated as: $\Phi_D = 3.2 \times 10^5 V_p^{4/3} B_{yz} \sin^{9/2}(\theta/2)$ (Milan et al., 2012). In these expressions, $B_{yz} = \sqrt{B_y^2 + B_z^2}$, B_y and B_z are the IMF components, and θ is the IMF clock angle.

2.5 The geomagnetic database

The geomagnetic conditions are explored by the 1-min resolution SYM-H index (Iyemori, 1990) obtained from the World Data Center for Geomagnetism, Kyoto, Japan, and the westward auroral electrojet proxy SML (at 1-min resolution) obtained from the SuperMAG database (Gjerloev, 2009). The SYM-H index is considered a proxy for the equatorial geomagnetic ring current (Dessler & Parker, 1959; Sckopke, 1966). A geomagnetic storm is identified by the criterion: SYM-H ≤ -50 nT (Gonzalez et al., 1994). On the other hand, SML intensifications are associated with substorm-related auroral ionospheric westward currents. The substorm occurrence times are obtained from a SuperMAG substorm list (Ohtani & Gjerloev, 2020).

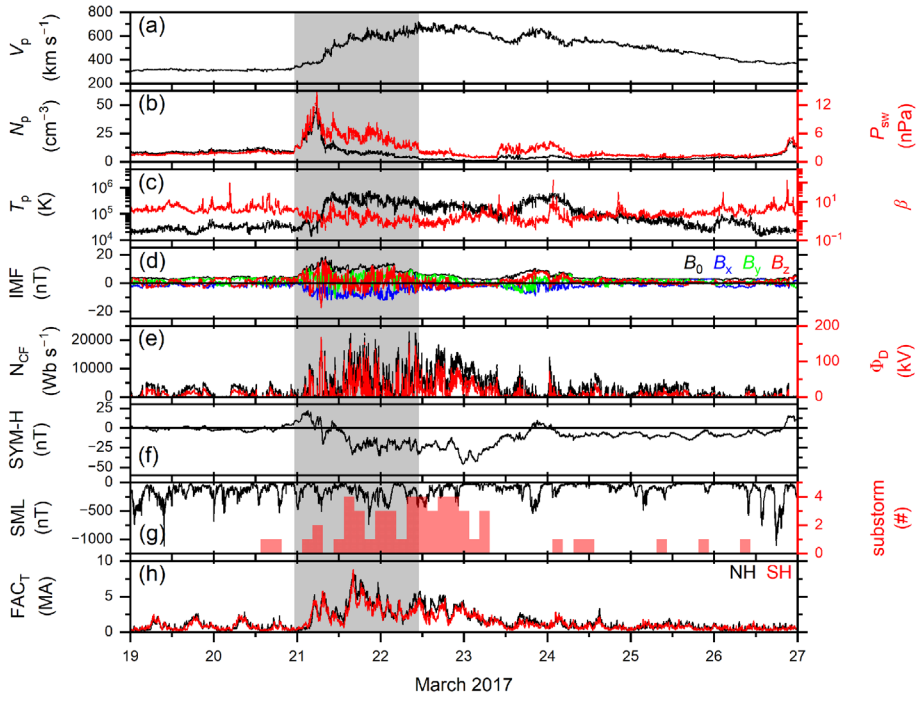

Figure 1. Solar wind, geomagnetic conditions, and FACs associated with a solar wind HSS during 19–26 March 2017. From top to bottom, the panels are: (a) solar wind proton speed V_p, (b) proton density N_p (black, legend on the left) and ram pressure P_{sw} (red, legend on the right), (c) proton temperature T_p (black, legend on the left) and plasma-β (red, legend on the right), (d) interplanetary magnetic field (IMF) magnitude B_0, and B_x, B_y, and B_z components, (e) the Newell coupling function N_{CF} (black, legend on the left) and dayside magnetic reconnection rate Φ_D (red, legend on the right), (f) symmetric ring current index SYM-H, (g) westward auroral electrojet index SML (black, legend on the left) and number of substorms in each 3-h interval (red, legend on the right), and (h) total FAC intensity (FAC_T) in the northern hemisphere (NH; black) and southern hemisphere (SH; red). Vertical shading indicates a CIR.

2.6 Periodicity analyses

Periodic variations of the FACs, solar wind, and geomagnetic parameters are studied by the Lomb-Scargle periodogram analysis (Lomb 1976; Scargle 1982), which is a suitable tool for identifying the significant periodicities in unequally spaced data. We applied cross-wavelet transform (XWT), which provides a dynamic energy correlation between two time series (Grinsted et al., 2004; see also Souza et al., 2016, 2018; Hajra et al., 2021, 2023 for detailed definitions, descriptions and examples). In addition, XWT coherence is computed to study the relationship between the two parameters. As we are interested in long-term relationships, all data for XWT and coherence analyses are processed into 30-min resolution by taking 30-min running averages so that they precisely coincide (in time) with each other.

3 Results

Figure 1 shows an example of a solar wind HSS, associated geomagnetic variations, and FAC intensities during 19–26 March 2017. From the solar wind V_p temporal variation, an HSS is identified with a peak V_p of ~719 km s^{-1} at ~10:56 UT on 22 March (Fig. 1a). The peak is preceded by a gradual rise at ~3.4 m s^{-2} and is followed by a slower decay at ~1.0 m s^{-2}. Considering a propagation time of ~2.4 days (from the Sun to Earth) of the V_p ~ 719 km s^{-1} HSS, a large, long-lasting coronal hole identified at the Sun on 20 March is determined to be the solar source of the HSS. The coronal hole is shown in Figure 2a. From solar synoptic analysis (Fig. 2b), the coronal hole has a positive polarity (i.e., magnetic field pointing away from the Sun). The polarity is consistent with the anti-sunward IMF direction, as evident from negative B_x and positive B_y components of IMF during the HSS (Fig. 1d). Large fluctuations in the IMF polarity (highly correlated to the plasma velocity components, not shown) during the HSS are a signature of interplanetary Alfvén waves (Coleman 1966; Belcher & Davis, 1971; Neugebauer et al., 1984). The proton temperature T_p (Fig. 1c) follows the V_p temporal profile in the HSS.

The interaction region between the HSS and a slow stream with V_p of ~310–320 km s^{-1} (identified on 19–20 March) is characterized by enhanced peak N_p (~53 cm^{-3}, Fig. 1b), P_{sw} (~15 nPa, Fig. 1b), and IMF B_0 (~19 nT, Fig. 1d), representing plasma and magnetic field compressions inside a CIR.

The CIR and the HSS proper are characterized by enhanced magnetopause reconnection rate (Φ_D, Fig. 1e) and consequent magnetic flux opening rate (N_{CF}, Fig. 1e), leading to increases in the ring current (Fig. 1f) and auroral substorm activities (Fig. 1g) compared to the pre-CIR interval. While SML variation shows enhancement of substorm-related westward current intensity, the number of substorm occurrences in each 3-h interval substantially increased during the interval of high Φ_D and

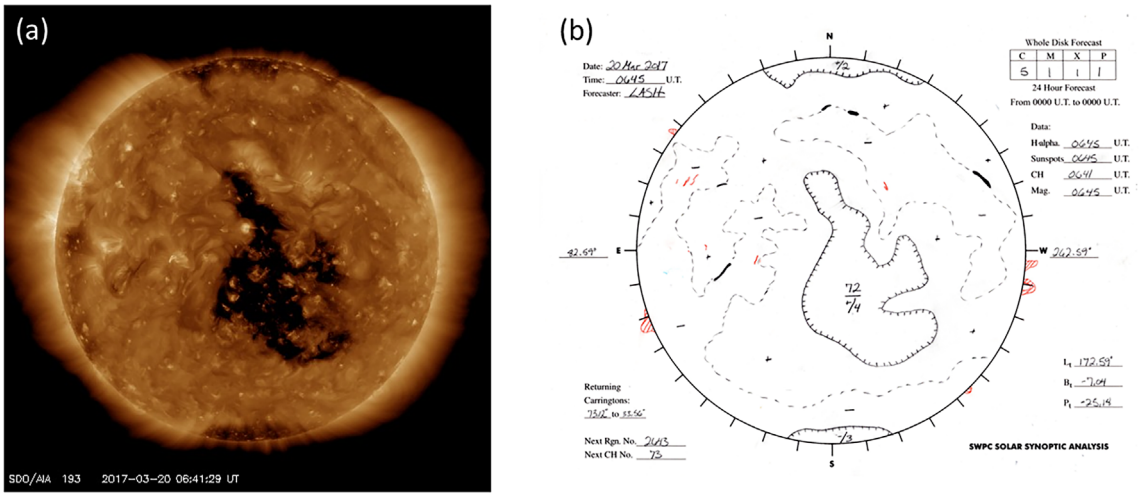

Figure 2. Coronal hole identified on 20 March 2017. (a) Solar image taken by NASA's SDO/AIA telescope at the wavelength of 193 Å. The dark region around the center of the image is a coronal hole. (b) Solar synoptic map. The coronal hole is assigned NOAA number 72 and is characterized by a positive polarity magnetic field.

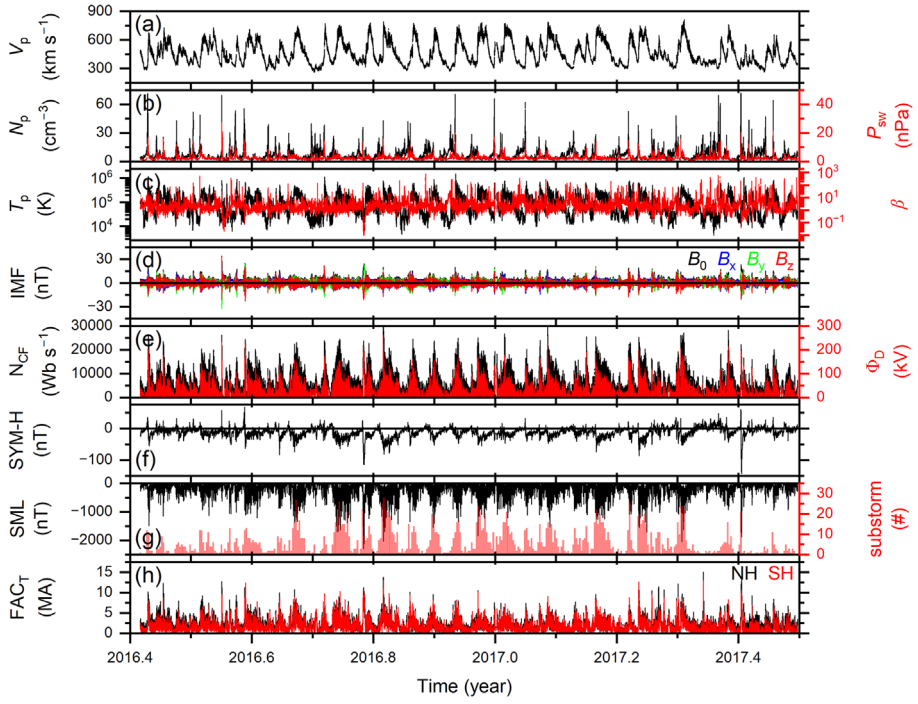

Figure 3. Solar wind, geomagnetic indices/conditions, and FAC intensities from 1 June 2016 through 30 June 2017. The panels are in the same format as in Figure 1.

N_{CF}. However, the peak SYM-H is –46 nT, above the geomagnetic storm threshold (SYM-H $\leq$ –50 nT). This is consistent with the weaker geoeffectiveness of CIRs in causing geomagnetic storms (Tsurutani et al., 1995; see Tsurutani et al., 2024 for a discussion and an exception). Following the CIR onset, the total FAC intensities (FAC$_T$) increased to a peak of ~9 MA from a pre-CIR value of ~2 MA in both northern and southern hemispheres (Fig. 1h).

Figure 3 shows near-Earth solar wind conditions, geomagnetic and auroral responses, and FAC intensity variations from 1 June 2016 through 30 June 2017. Variation of V_p is characterized by multiple peaks (Fig. 3a). Analysis of individual peaks, associated plasma (Figs. 3a–3c), IMF parameters (Fig. 3d), and solar images (as described above) identifies thirty-three HSSs emanated from solar coronal holes. The HSS peak V_p values, their occurrence times, and magnetic polarities are listed in

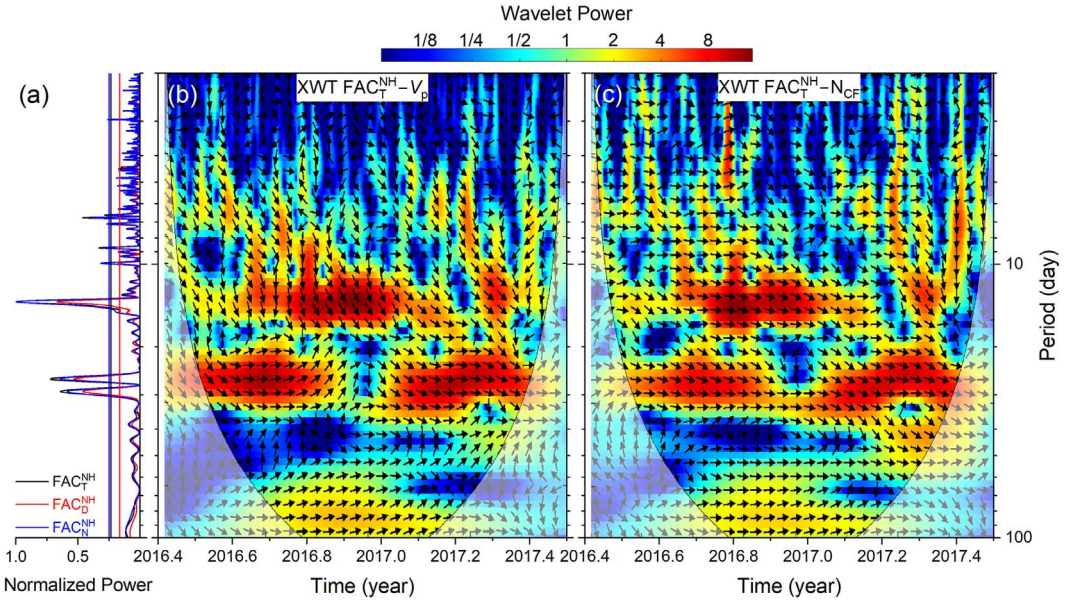

Figure 4. Periodogram analyses of FAC intensity and solar wind coupling. (a) Lomb-Scargle periodograms of the northern hemispheric total (black), dayside (red), and nightside (blue) FAC intensities; T represents total, D is dayside, N is nightside, NH is the northern hemisphere; and 95% confidence levels of the three periodograms are shown by three vertical lines. Cross-wavelet transforms of (b) northern hemispheric total FAC intensity and V_p, and (c) northern hemispheric total FAC intensity and N_{CF}. Wavelet powers are shown by the color bar at the top. The cone of influence, where edge effects might distort the results, is shown in lighter shades. The relative phase relationships (of FAC intensity with V_p and N_{CF}) are shown as arrows, horizontal right arrows indicating in-phase, horizontal left arrows indicating anti-phase. For the Lomb-Scargle periodograms, 2-min resolution FAC intensities are used, while for cross-wavelets, all data are processed into 30-min resolution (by taking 30-min running averages) so that they precisely coincide (in time) with each other.

Table A1. We also identified two ICMEs during this interval. Descriptions of the ICMEs and associated FAC intensity variations are given in the Figures B1 and B2. The ICMEs are not included in the analyses that follow.

The HSS V_p peaks vary between ∼486 and ∼818 km s^{-1}, with an average (median) V_p of ∼704 ± 78 (∼728) km s^{-1} for all HSSs (the number following the ± symbol is 1-σ deviation, which is only ∼11% of the average V_p). Note that an HSS emanated from a polar coronal hole is assumed to have a peak V_p ∼ 750–800 km s^{-1} (e.g., McComas et al., 2000). The lesser speeds recorded here are due to superradial expansion effects at the edges of the HSSs. The V_p peaks are preceded by peaks in N_p (Fig. 3b), P_{sw} (Fig. 3b), and IMF B_0 (Fig. 3d), associated with plasma and IMF compressions in CIRs. All of the CIRs are associated with intensifications of the coupling functions N_{CF} and Φ_D (Fig. 3e), ring current index SYM-H (Fig. 3f), number of substorms and SML intensity (Fig. 3g), and FAC$_T$ (Fig. 3h). These are consistent with the case study shown in Figure 1. Figure 3 clearly demonstrates the influence of repeating/periodic/recurring HSS impingements on the Earth's magnetosphere-ionosphere system, as reflected in variations of the geomagnetic indices and currents.

Figure 4a shows Lomb-Scargle periodograms of the northern hemispheric FAC intensities (similar periodograms for solar wind parameters, coupling functions, auroral indices, and southern hemispheric FAC intensities are shown in Fig. C1). The FAC intensity periodograms are characterized by the strongest peak at ∼13.8 days, followed by two weaker peaks at ∼26.2 and ∼29.2 days (both of the latter peaks are essentially at ∼27 days). The periodicities are generally the same for dayside, nightside, and total FAC intensities in both the northern and southern hemispheres.

Figures 4b and 4c show cross-wavelets of total northern hemispheric FAC intensity with V_p and N_{CF}, respectively. Phase differences of FAC intensity with V_p and N_{CF} are indicated by the arrows, rightward-pointing (leftward-pointing) horizontal arrows indicating the in-phase (anti-phase) relationship. Based on the spectral power, the strongest common period for FAC intensity and V_p, as well as for FAC intensity and N_{CF}, is centered around 28 days, followed by another peak at ∼14 days. Both peaks have "intermittent" distributions. While the ∼28-day period is observed from around 18 June 2016 through 27 November 2016 (∼2016.47–2016.91) and from around 23 December 2016 through 7 June 2017 (∼2016.98–2017.43), the ∼14-day period is most prominent from around 4 August 2016 through 7 March 2017 (∼2016.59–2017.18). The existence of common periodicities between FAC intensity and V_p, and between FAC intensity and N_{CF}, is indicative of the close relationships of FAC intensity with V_p and N_{CF}.

The phase relationship of FAC intensities with V_p is different from that with N_{CF}. While FAC intensities are mostly in-phase with V_p around the 28-day periodicity, phase differences between the two are prominent at a ∼14-day period (Fig. 4b). On the contrary, FAC intensities are almost in-phase with N_{CF} at both ∼28 and ∼14-day periodicities (Fig. 4c). However, slight differences in phase (between FAC intensity and N_{CF}) are indicated by slightly downward-pointing arrows. This slightly out-of-phase relationship is consistent with a certain

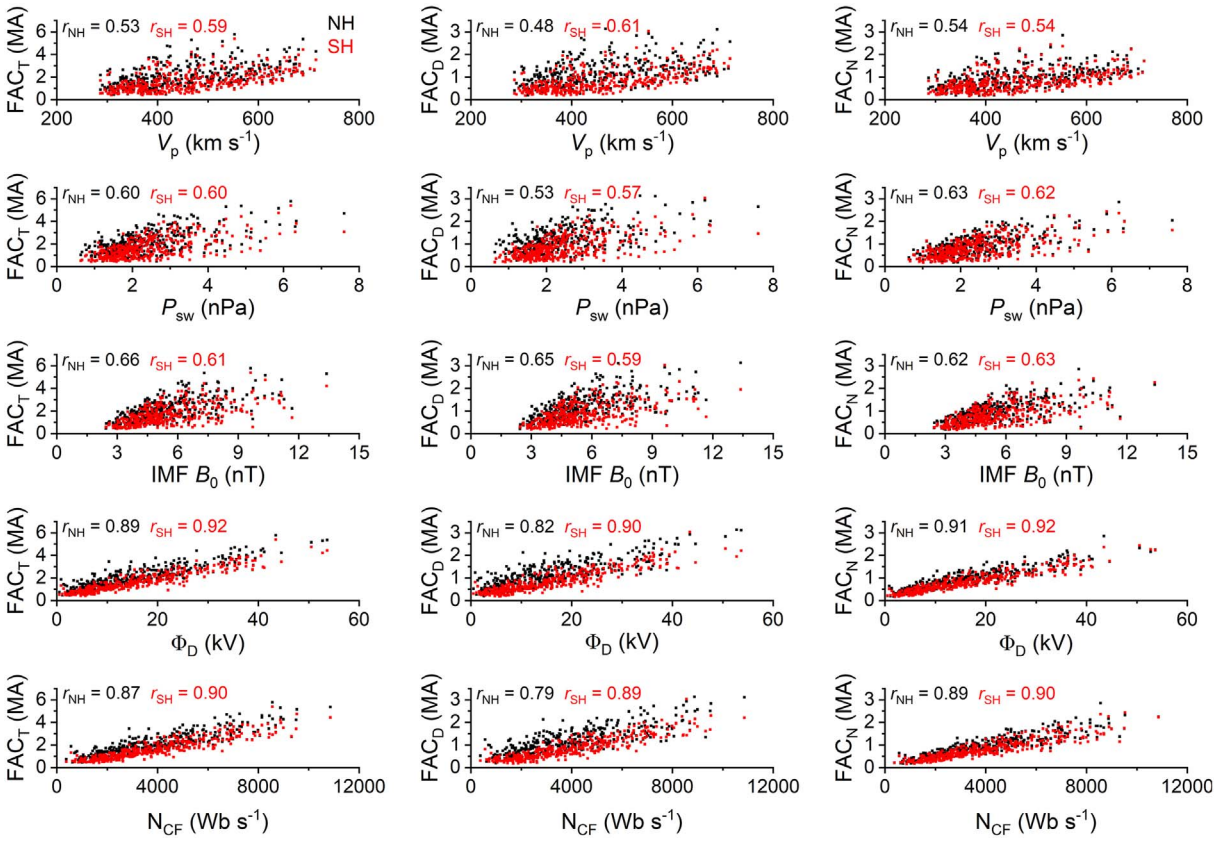

Figure 5. Variations of FAC intensities FAC_T (left column), FAC_D (middle column), and FAC_N (right column) with solar wind plasma, IMF, and solar wind-magnetosphere coupling functions V_p, P_{sw}, IMF B_0, Φ_D, and N_{CF} (from top to bottom panels). In each panel, black and red data correspond to the northern (NH) and southern (SH) hemispheric FACs, respectively. Pearson's linear correlation coefficients (r) obtained from linear regression analyses are mentioned in each panel. The statistical significance of the correlation coefficients is confirmed by the Student's t-test (Student. 1908).

(∼40–60 min) delay between the solar wind driving and the FAC intensity, as reported before (e.g., Pedersen et al., 2023). The minutes-to-hour scale time lags are not further explored as we are interested in longer scale trends in FACs. In addition, FAC intensity exhibits enhanced wavelet coherence with V_p around the ∼28 and ∼14-day periodicities, and with N_{CF} for almost all periods (see Fig. C2).

Relationships of FAC intensities with solar wind plasma, IMF, and solar wind-magnetosphere coupling functions are further explored in Figure 5. They show variations of daily mean total FAC intensity (FAC_T), dayside FAC intensity (FAC_D) and nightside FAC intensity (FAC_N) in the northern (NH) and southern (SH) hemispheres with daily mean solar wind parameters and coupling functions (daily mean values are used as we are interested in long-term trends in FAC variations). All panels show linearly increasing trends in FAC_T, FAC_D, and FAC_N with increasing solar wind parameters and coupling functions. Pearson's correlation coefficients obtained from the linear regression analysis are mentioned in each panel.

While correlations with FACs are weaker for V_p, P_{sw}, IMF B_0 (r = 0.48–0.66), stronger correlations are noted with the coupling functions Φ_D (r = 0.82–0.92) and N_{CF} (r = 0.79–0.90). FAC_N exhibits a stronger correlation than FAC_D, and correlations are slightly stronger for southern hemispheric FACs than for northern hemispheric FACs.

4 Discussion

We have presented the first observations of periodic variations of FAC intensities in response to recurrent solar wind HSSs during a solar cycle minimum condition. Both dayside and nightside FAC intensities in both the northern and southern hemispheres are characterized by distinct periodicities of ∼14, ∼26, and ∼29 days.

It may be worth noting that Hajra et al. (2025a) reported ∼19 and ∼11 h periodicities in FAC intensities during HILD-CAAs lasting for a few days to a week. The periodicities were attributed to interplanetary Alfvén waves (Korth et al., 2011; Tsurutani et al., 2006a). On the other hand, Hajra et al. (2025c) identified a ∼1-year periodicity in solar cycle variation of FACs, which is not plausible to be driven by solar winds.

The solar activity minimum period is characterized by low solar ionizing fluxes (thus low ionospheric conductance) as well as low occurrences of solar transient activity such as solar flares and ICMEs (thus low occurrence of strong magnetospheric convection). However, cross-wavelet and coherence analyses confirmed causal relationships of FAC intensity variations with solar wind speed and solar wind-magnetosphere coupling. They are found to exhibit common periodicities centered around 14 and 27 days. The ∼26 and ∼29-day periodicities in FACs are close to the ∼27-day solar rotation period, and we assume that

they are essentially the same peak. The ~14-day FAC periodicity represents the first harmonic of the solar rotation period (Gosling et al., 1976; Zirker 1977; Lindblad & Lundstedt, 1981). The appearance of well-separated spectral peaks at ~26 and ~29 days may suggest an amplitude modulation of the FAC intensity, varying with the solar rotation period.

Modulation of FAC intensities by solar wind HSSs is statistically confirmed by significant linear correlations of both dayside and nightside FAC intensities with solar wind/interplanetary parameters and coupling functions. Correlations of FACs with solar wind-magnetosphere coupling functions are consistent with previous studies of FACs, but during auroral substorms (e.g., Coxon et al., 2014a), geomagnetic storms (e.g., Pedersen et al., 2023), and HILDCAAs (Hajra et al., 2025a). HSSs convect interplanetary Alfvén waves, the southward component of which causes magnetic reconnection at the dayside magnetopause (Dungey 1961). HSSs can also cause viscous interaction at the dayside magnetopause (Axford & Hines, 1961). Both of these processes are believed to lead to substorm activity. Clearly, the nightside FACs are associated with substorms (Coxon et al., 2014a, 2014b; Pedersen et al., 2021, 2022; Zhong et al., 2022; Wang et al., 2024; Hajra et al., 2025c).

However, it is possible that the dayside FACs are separate and distinct from the nightside substorm FAC events. Previous studies have revealed that dayside FAC intensities are controlled by ionospheric conductance (Fujii et al., 1981; Wang et al., 2005; Coxon et al., 2016; Hajra et al., 2025c). However, Tsurutani et al. (2001) showed that the dayside and nightside polar cap boundary layer waves were continuously connected in a 24-h local time oval. While ionospheric conductance varies with seasons due to solar irradiance variations, our results suggest that dayside FACs are also associated with either magnetic reconnection, viscous interaction, or both. This is consistent with recent studies (Zhong et al., 2022; Wang & Lühr, 2023; Wang et al., 2024) indicating that energetic particle precipitation may enhance the auroral ionospheric Hall conductance.

As expected, the FAC intensity exhibits better correlation with the coupling functions (Φ_D and N_{CF}) than with solar wind plasma and IMF parameters (V_p, P_{sw}, IMF B_0). In addition, FAC intensity exhibits better phase relationship with N_{CF} than with V_p at the ~14-day periodicity. These results may be related to the fact that the higher values of N_{CF} and FAC intensity are observed during the compression regions (CIRs) rather than during the HSSs. In other words, the physical driver of the FAC intensity modulation appears to be N_{CF}, signifying enhanced solar wind-magnetosphere coupling in CIRs. Lower correlation with solar wind/IMF parameters (and higher correlation with coupling functions) may indicate combined roles of the plasma/IMF characteristic parameters in controlling geophysical processes.

5 Final comment

This study interval, June 2016 to June 2017, occurred during the solar activity minimum between solar cycles 24 and 25. It is noted that the interval was dominated by periodic (~27-day) solar wind HSSs which reached peak speeds of ~820 km s^{-1}. In a previous work, Tsurutani et al. (2011) studied the solar wind and geomagnetic activity during the two previous solar minima between solar cycles 22 and 23, and between solar cycles 23 and 24. Due to the solar location of coronal holes during the previous two solar minima, the solar wind HSSs never approached their maximum speeds of ~820 km s^{-1} as shown in this 2016–2017 solar minimum. The two previous extreme minima in geomagnetic activity essentially established a ground state of the magnetosphere. We suggest that future studies of extreme solar minima be performed, which may allow resolution of some of the uncertainties in the physical causes of dayside and nightside FACs indicated in this paper.

Acknowledgments

We would like to acknowledge Aslak Grinsted for providing the wavelet coherence package used in this work, available at http://noc.ac.uk/using-science/crosswavelet-wavelet-coherence. We would like to thank the editors and reviewers for sharing extremely valuable suggestions, which substantially improved the manuscript. The editor thanks Hermann Lühr and an anonymous reviewer for their assistance in evaluating this paper.

Funding

The work of RH is funded by the "Hundred Talents Program" of the Chinese Academy of Sciences (CAS), the "Excellent Young Scientists Fund Program (Overseas)", and the "Research Fund for International Excellent Young Scientists" (grant number: W2532030) of the National Natural Science Foundation of China (NSFC). AMSF would like to thank the Institute of Geosciences and Engineering-UNIFESSPA (project n°. 23479.009478/2024-60). EE would like to thank the Brazilian agency CNPq for research grants (contract PQ-301883/2019-0 and PQ-303900-2024-5).

Conflicts of interests

The authors declare no financial and non-financial competing interests.

Data availability statement

The FAC data are obtained from the AMPERE Science Data Center of the Johns Hopkins Applied Physics Laboratory (https://ampere.jhuapl.edu/). The data is available for free download from the AMPERE Derived Product Data Files (Daily) page (https://ampere.jhuapl.edu/download/?page=derivedProductsTab). The near-Earth solar wind plasma and IMF data are obtained from NASA's OMNIWeb Plus database (https://omniweb.gsfc.nasa.gov/). The high-resolution data can be downloaded directly from the page: https://omniweb.gsfc.nasa.gov/form/omni_min.html, by specifying start and stop times. The solar SDO/AIA images are obtained from https://sdo.gsfc.nasa.gov/, and the NOAA solar synoptic maps are obtained from http://www.swpc.noaa.gov/. Geomagnetic SYM-H indices are obtained from the World Data Center for Geomagnetism, Kyoto, Japan (http://wdc.kugi.kyoto-u.ac.jp/). The indices can be freely downloaded from the "Plot and data output of ASY/SYM and AE indices" (https://wdc.kugi.kyoto-u.ac.jp/aeasy/index.html) by specifying start time and duration. The SML indices are obtained from the SuperMAG website (https://supermag.jhuapl.edu/). They can be freely downloaded from the Indices (https://supermag.jhuapl.edu/indices/) by specifying the index, time, and duration. The SuperMAG substorm list is collected from the Products (https://supermag.jhuapl.edu/products/?tab=download) by specifying the start and end times, and Substorm List as "Ohtani & Gjerloev, 2020".

Author contribution statement

Conceptualization: RH, BTT; Methodology: RH; Validation: RH, BTT; Formal analysis: RH, AMSF; Investigation: RH, BTT; Resources: RH; Data Curation: RH; Visualization: RH; Supervision: RH, BTT; Funding acquisition: RH. Writing – Original Draft: RH; Writing – Review & Editing: RH, BTT, AMSF, QL, AD, GSL, SL, XG, EE. All authors read and approved the final manuscript.

References

Alves, MV, Echer E, Gonzalez WD. 2006. Geoeffectiveness of corotating interaction regions as measured by *Dst* index. *J. Geophys. Res. Space Physics* **111**: 2005JA011379. https://doi.org/10.1029/2005JA011379.

Anderson, BJ, Takahashi K, Kamei T, Waters CL, Toth BA. 2002. Birkeland current system key parameters derived from Iridium observations: Method and initial validation results. *J. Geophys. Res. Space Physics* **107**: SMP 11-1-SMP 11-13. https://doi.org/10.1029/2001JA000080.

Araki, T, Funato K, Iguchi T, Kamei T. 1993. Direct detection of solar wind dynamic pressure effect on ground geomagnetic field. *Geophys. Res. Lett.* **20**: 775–778. https://doi.org/10.1029/93GL00852.

Axford, WI, Hines CO. 1961. A unifying theory of high-latitude geophyaical phenomena and geomagnetic storms. *Can. J. Phys.* **39**: 1433–1464. https://doi.org/10.1139/p61-172.

Baker, KB, Wing S. 1989. A new magnetic coordinate system for conjugate studies at high latitudes. *J. Geophys. Res.* **94**: 9139–9143. https://doi.org/10.1029/JA094iA07p09139.

Belcher, JW, Davis L. 1971. Large-amplitude Alfvén waves in the interplanetary medium, 2. *J. Geophys. Res.* **76**: 3534–3563. https://doi.org/10.1029/JA076i016p03534.

Birkeland, K. 1908. *The Norwegian Aurora Polaris Expedition, 1902-1903* (Vol. **1**). H. Aschelhoug, Christiania. https://doi.org/10.5962/bhl.title.17857.

Burlaga, LF, Sittler E, Mariani F, Schwenn R. 1981. Magnetic loop behind an interplanetary shock: Voyager, Helios, and IMP 8 observations. *J. Geophys. Res. Space Physics* **86**: 6673–6684. https://doi.org/10.1029/JA086iA08p06673.

Chi, Y, Shen C, Luo B, Wang Y, Xu M. 2018. Geoeffectiveness of Stream Interaction Regions From 1995 to 2016. *Space Weather* **16**: 1960–1971. https://doi.org/10.1029/2018SW001894.

Coleman, PJ. 1966. Hydromagnetic Waves in the Interplanetary Plasma. *Phys. Rev. Lett.* **17**: 207–211. https://doi.org/10.1103/PhysRevLett.17.207.

Coxon, JC, Milan SE, Clausen LBN, Anderson BJ, Korth H. 2014a. A superposed epoch analysis of the regions 1 and 2 Birkeland currents observed by AMPERE during substorms. *J. Geophys. Res. Space Physics* **119**: 9834–9846. https://doi.org/10.1002/2014JA020500.

Coxon, JC, Milan SE, Clausen LBN, Anderson BJ, Korth H. 2014b. The magnitudes of the regions 1 and 2 Birkeland currents observed by AMPERE and their role in solar wind-magnetosphere-ionosphere coupling. *J. Geophys. Res. Space Physics* **119**: 9804–9815. https://doi.org/10.1002/2014JA020138.

Coxon, JC, Milan SE, Carter JA, Clausen LBN, Anderson BJ, et al. 2016. Seasonal and diurnal variations in AMPERE observations of the Birkeland currents compared to modeled results. *J. Geophys. Res. Space Physics* **121**: 4027–4040. https://doi.org/10.1002/2015JA022050.

Dessler, AJ, Parker EN. 1959. Hydromagnetic theory of geomagnetic storms. *J. Geophys. Res.* **64**: 2239–2252. https://doi.org/10.1029/JZ064i012p02239.

Dungey, JW. 1961. Interplanetary Magnetic Field and the Auroral Zones. *Phys. Rev. Lett.* **6**: 47–48. https://doi.org/10.1103/PhysRevLett.6.47.

Fujii, R, Iijima T, Potemra TA, Sugiura M. 1981. Seasonal dependence of large-scale Birkeland currents. *Geophys. Res. Lett.* **8**: 1103–1106. https://doi.org/10.1029/GL008i010p01103.

Gjerloev, JW. 2009. A global ground-based magnetometer initiative. *EOS Trans. Am. Geophys. Union* **90**: 230–231. https://doi.org/10.1029/2009EO270002.

Gonzalez, WD, Tsurutani BT. 1987. Criteria of interplanetary parameters causing intense magnetic storms (Dst < −100 nT). *Planet Space Sci* **35**: 1101–1109. https://doi.org/10.1016/0032-0633(87)90015-8.

Gonzalez, WD, Joselyn JA, Kamide Y, Kroehl HW, Rostoker G, et al. 1994. What is a geomagnetic storm? *J. Geophys. Res. Space Physics* **99**: 5771–5792. https://doi.org/10.1029/93JA02867.

Gosling, JT, Asbridge JR, Bame SJ, Feldman WC. 1976. Solar wind speed variations: 1962-1974. *J. Geophys. Res.* **81**: 5061–5070. https://doi.org/10.1029/JA081i028p05061.

Grinsted, A, Moore JC, Jevrejeva S. 2004. Application of the cross wavelet transform and wavelet coherence to geophysical time series. *Nonlinear Process. Geophys.* **11**: 561–566. https://doi.org/10.5194/npg-11-561-2004.

Hajra, R. 2021. Seasonal dependence of the Earth's radiation belt – new insights. *Ann. Geophys.* **39**: 181–187. https://doi.org/10.5194/angeo-39-181-2021.

Hajra, R, Tsurutani BT. 2018. Magnetospheric "Killer" Relativistic Electron Dropouts (REDs) and Repopulation: A Cyclical Process. In *Extreme Events in Geospace* (pp. 373–400). Elsevier. https://doi.org/10.1016/B978-0-12-812700-1.00014-5.

Hajra, R, Echer E, Tsurutani BT, Gonzalez WD. 2013. Solar cycle dependence of High-Intensity Long-Duration Continuous AE Activity (HILDCAA) events, relativistic electron predictors? *J. Geophys. Res. Space Physics* **118**: 5626–5638. https://doi.org/10.1002/jgra.50530.

Hajra, R, Tsurutani BT, Echer E, Gonzalez WD. 2014a. Relativistic electron acceleration during high-intensity, long-duration, continuous *AE* activity (HILDCAA) events: Solar cycle phase dependences: Relativistic electrons during HILDCAAs. *Geophys. Res. Lett.* **41**: 1876–1881. https://doi.org/10.1002/2014GL059383.

Hajra, R, Echer E, Tsurutani BT, Gonzalez WD. 2014b. Superposed epoch analyses of HILDCAAs and their interplanetary drivers: Solar cycle and seasonal dependences. *J Atmos Sol Terr Phys* **121**: 24–31. https://doi.org/10.1016/j.jastp.2014.09.012.

Hajra, R, Tsurutani BT, Echer E, Gonzalez WD, Santolik O. 2015a. Relativistic (E > 0.6, > 2.0, and > 4.0 MeV) electron acceleration at geosynchronous orbit during high-intensity, long-duration, continuous AE activity (HILDCAA) events. *Astrophys. J.* **799**: 39. https://doi.org/10.1088/0004-637X/799/1/39.

Hajra, R, Tsurutani BT, Echer E, Gonzalez WD, Brum CGM, et al. 2015b. Relativistic electron acceleration during HILDCAA events: are precursor CIR magnetic storms important? *Earth Planet Space* **67**: 109. https://doi.org/10.1186/s40623-015-0280-5.

Hajra, R, Franco AMS, Echer E, Bolzan MJA. 2021. Long-term variations of the geomagnetic activity: a comparison between the strong and weak solar activity cycles and implications for the space climate. *J. Geophys. Res. Space Physics* **126**: e2020JA028695. https://doi.org/10.1029/2020JA028695.

Hajra, R, Echer E, Franco AMS, Bolzan MJA. 2023. Earth's magnetotail variability during supersubstorms (SSSs): A study on

solar wind–magnetosphere–ionosphere coupling. *Adv. Space Res.* **72**: 1208–1223. https://doi.org/10.1016/j.asr.2023.04.013.

Hajra, R, Tsurutani BT, Lakhina GS, Lu Q, Du A. 2024a. Interplanetary Causes and Impacts of the 2024 May Superstorm on the Geosphere: An Overview. *Astrophys. J.* **974**: 264. https://doi.org/10.3847/1538-4357/ad7462.

Hajra, R, Tsurutani BT, Lu Q, Horne RB, Lakhina GS, et al. 2024b. The April 2023 SYM-H = −233 nT Geomagnetic Storm: A Classical Event. *J. Geophys. Res. Space Physics* **129**: e2024JA032986. https://doi.org/10.1029/2024JA032986.

Hajra, R, Tsurutani BT, Lu Q, Lakhina GS., Du A, et al. 2024c. Ultra-relativistic Electron Acceleration during High-intensity Long-duration Continuous Auroral Electrojet Activity Events. *Astrophys. J.* **965**: 146. https://doi.org/10.3847/1538-4357/ad2dfe.

Hajra, R, Tsurutani BT, Lu Q, Du A, Lu S, et al. 2025a. Field-Aligned Currents during High-Intensity Long-Duration Continuous Auroral Electrojet Activity Events: A Statistical Study. *Space Weather* **23**: e2025SW004353. https://doi.org/10.1029/2025SW004353.

Hajra, R, Tsurutani BT, Lu Q, Du A. 2025b. Field-Aligned Currents during High-Intensity Long-Duration Continuous Auroral Electrojet Activity Events: Seasonal Dependences. *Space Weather* **23**: e2025SW004354. https://doi.org/10.1029/2025SW004354.

Hajra, R, Tsurutani BT, Lu Q, Du A, Lu S, et al. 2025c. Solar cycle and seasonal dependences of field-aligned currents. *Space Weather* **23**: e2025SW004441. https://doi.org/10.1029/2025SW004441.

Iijima, T, Potemra TA. 1976. The amplitude distribution of field-aligned currents at northern high latitudes observed by Triad. *J. Geophys. Res.* **81**: 2165–2174. https://doi.org/10.1029/JA081i013p02165.

Iijima, T, Potemra TA. 1978. Large-scale characteristics of field-aligned currents associated with substorms. *J. Geophys. Res. Space Physics* **83**: 599–615. https://doi.org/10.1029/JA083iA02p00599.

Iyemori, T. 1990. Storm-time magnetospheric currents inferred from mid-latitude geomagnetic field variations. *J. Geomagn. Geoelectr.* **42**: 1249–1265. https://doi.org/10.5636/jgg.42.1249.

Kennel, CF, Edmiston JP, Hada T. 1985. A Quarter Century of Collisionless Shock Research. In RG Stone, BT Tsurutani (Eds.), *Geophys Mono Ser,* Am Geophys Union, Washington, D.C., pp. 1–36. https://doi.org/10.1029/GM034p0001.

King, JH, Papitashvili NE. 2020. OMNI 1-min Data Set [Data set]. *NASA Space Physics Data Facility.* https://doi.org/10.48322/45BB-8792.

Knipp, DJ, Matsuo T, Kilcommons L, Richmond A, Anderson B, et al. 2014. Comparison of magnetic perturbation data from LEO satellite constellations: Statistics of DMSP and AMPERE. *Space Weather* **12**: 2–23. https://doi.org/10.1002/2013SW000987.

Korth, A, Echer E, Zong QG, Guarnieri FL, Fraenz M, et al. 2011. The response of the polar cusp to a high-speed solar wind stream studied by a multispacecraft wavelet analysis. *J Atmos Sol Terr Phys* **73**: 52–60. https://doi.org/10.1016/j.jastp.2009.10.004.

Krieger, AS, Timothy AF, Roelof EC. 1973. A coronal hole and its identification as the source of a high velocity solar wind stream. *Sol. Phys.* **29**: 505–525. https://doi.org/10.1007/BF00150828.

Lakhina, GS, Tsurutani BT, Kojima H, Matsumoto H. 2000. "Broadband" plasma waves in the boundary layers. *J. Geophys. Res. Space Physics* **105**: 27791–27831. https://doi.org/10.1029/2000JA900054.

Lakhina, GS, Tsurutani BT, Singh SV, Reddy RV. 2003. Some theoretical models for solitary structures of boundary layer waves. *Nonlinear Process. Geophys.* **10**: 65–73. https://doi.org/10.5194/npg-10-65-2003.

Le, G, Lühr H, Anderson BJ, Strangeway RJ, Russell CT, et al. 2016. Magnetopause erosion during the 17 March 2015 magnetic storm: Combined field-aligned currents, auroral oval, and magnetopause observations. *Geophys. Res. Lett.* **43**: 2396–2404. https://doi.org/10.1002/2016GL068257.

Lindblad, BA, Lundstedt H. 1981. A catalogue of high-speed plasma streams in the solar wind. *Sol. Phys.* **74**: 197–206. https://doi.org/10.1007/BF00151290.

Lomb, NR. 1976. Least-squares frequency analysis of unequally spaced data. *Astrophys Space Sci* **39**: 447–462. https://doi.org/10.1007/BF00648343.

Lyons, LR, Gallardo-Lacourt B, Zou S, Weygand JM, Nishimura Y, et al. 2016. The 17 March 2013 storm: Synergy of observations related to electric field modes and their ionospheric and magnetospheric Effects. *J. Geophys. Res. Space Physics* **121**: 10880–10897. https://doi.org/10.1002/2016JA023237.

Marubashi, K, Lepping RP. 2007. Long-duration magnetic clouds: a comparison of analyses using torus- and cylinder-shaped flux rope models. *Ann. Geophys.* **25**: 2453–2477. https://doi.org/10.5194/angeo-25-2453-2007.

McComas, DJ, Barraclough BL, Funsten HO, Gosling JT, Santiago Muñoz E, et al. 2000. Solar wind observations over Ulysses' first full polar orbit. *J. Geophys. Res. Space Physics* **105**: 10419–10433. https://doi.org/10.1029/1999JA000383.

Milan, SE, Gosling JS, Hubert B. 2012. Relationship between interplanetary parameters and the magnetopause reconnection rate quantified from observations of the expanding polar cap. *J. Geophys. Res. Space Physics* **117**: 2011JA017082. https://doi.org/10.1029/2011JA017082.

Neugebauer, M, Clay DR, Goldstein BE, Tsurutani BT, Zwickl RD. 1984. A reexamination of rotational and tangential discontinuities in the solar wind. *J. Geophys. Res. Space Physics* **89**: 5395–5408. https://doi.org/10.1029/JA089iA07p05395.

Newell, PT, Sotirelis T, Liou K, Meng CI, Rich FJ. 2007. A nearly universal solar wind-magnetosphere coupling function inferred from 10 magnetospheric state variables. *J. Geophys. Res. Space Physics* **112**: 2006JA012015. https://doi.org/10.1029/2006JA012015.

Ohtani, S, Gjerloev JW. 2020. Is the Substorm Current Wedge an Ensemble of Wedgelets?: Revisit to Midlatitude Positive Bays. *J. Geophys. Res. Space Physics* **125**: e2020JA027902. https://doi.org/10.1029/2020JA027902.

Paulikas, GA, Blake JB. 1979. Effects of the Solar Wind on Magnetospheric Dynamics: Energetic Electrons at the Synchronous Orbit. In WP Olson (Ed.), *Geophys Mono Ser,*Am Geophys Union, Washington, D. C., pp. 180–202. https://doi.org/10.1029/GM021p0180.

Pedersen, MN, Vanhamäki H, Aikio AT, Käki S, Workayehu AB, et al. 2021. Field-aligned and ionospheric currents by AMPERE and SuperMAG during HSS/SIR-driven storms. *J. Geophys. Res. Space Physics* **126**: e2021JA029437. https://doi.org/10.1029/2021JA029437.

Pedersen, MN, Vanhamäki H, Aikio AT, Waters CL, Gjerloev JW, et al. 2022. Effect of ICME-Driven Storms on Field-Aligned and Ionospheric Currents From AMPERE and SuperMAG. *J. Geophys. Res. Space Physics* **127**: e2022JA030423. https://doi.org/10.1029/2022JA030423.

Pedersen, MN, Vanhamäki H, Aikio AT. 2023. Comparison of field-aligned current responses to HSS/SIR, sheath, and magnetic cloud driven geomagnetic storms. *Geophys. Res. Lett.* **50**: e2023GL103151. https://doi.org/10.1029/2023GL103151.

Scargle, JD. 1982. Studies in astronomical time series analysis. II - Statistical aspects of spectral analysis of unevenly spaced data. *Astrophys. J.* **263**: 835. https://doi.org/10.1086/160554.

Sckopke, N. 1966. A general relation between the energy of trapped particles and the disturbance field near the Earth. *J. Geophys. Res.* **71**: 3125–3130. https://doi.org/10.1029/JZ071i013p03125.

Smith, EJ, Wolfe JH. 1976. Observations of interaction regions and corotating shocks between one and five AU: Pioneers 10 and 11. *Geophys. Res. Lett.* **3**: 137–140. https://doi.org/10.1029/GL003i003p00137.

Souza, AM, Echer E, Bolzan MJA, Hajra R. 2016. A study on the main periodicities in interplanetary magnetic field Bz component and geomagnetic AE index during HILDCAA events using wavelet analysis. *J Atmos Sol Terr Phys*. **149**: 81–86. https://doi.org/10.1016/j.jastp.2016.09.006.

Souza, AM, Echer E, Bolzan MJA, Hajra R. 2018. Cross-correlation and cross-wavelet analyses of the solar wind IMF Bz and auroral electrojet index AE coupling during HILDCAAs. *Ann. Geophys.* **36**: 205–211. https://doi.org/10.5194/angeo-36-205-2018.

Student. 1908. The Probable Error of a Mean. *Biometrika* **6**: 1. https://doi.org/10.2307/2331554.

Tanskanen, EI, Slavin JA, Tanskanen AJ, Viljanen A, Pulkkinen TI, et al. 2005. Magnetospheric substorms are strongly modulated by interplanetary high-speed streams. *Geophys. Res. Lett.* **32**: 2005GL023318. https://doi.org/10.1029/2005GL023318.

Tsurutani, BT, Gonzalez WD. 1987. The cause of high-intensity long-duration continuous AE activity (HILDCAAs): Interplanetary Alfvén wave trains. *Planet Space Sci*. **35**: 405–412. https://doi.org/10.1016/0032-0633(87)90097-3.

Tsurutani, BT, Lakhina GS. 2014. An extreme coronal mass ejection and consequences for the magnetosphere and Earth. *Geophys. Res. Lett.* **41**: 287–292. https://doi.org/10.1002/2013GL058825.

Tsurutani, BT, Gonzalez WD, Tang F, Akasofu SI, Smith EJ. 1988. Origin of interplanetary southward magnetic fields responsible for major magnetic storms near solar maximum (1978–1979). *J. Geophys. Res. Space Physics* **93**: 8519–8531. https://doi.org/10.1029/JA093iA08p08519.

Tsurutani, BT, Gonzalez WD, Gonzalez ALC, Tang F, Arballo JK, et al. 1995. Interplanetary origin of geomagnetic activity in the declining phase of the solar cycle. *J. Geophys. Res. Space Physics* **100**: 21717–21733. https://doi.org/10.1029/95JA01476.

Tsurutani, BT, Lakhina GS, Ho CM, Arballo, JK, Galvan C, et al. 1998. Broadband plasma waves observed in the polar cap boundary layer: Polar. *J. Geophys. Res. Space Physics* **103**: 17351–17366. https://doi.org/10.1029/97JA03063.

Tsurutani, BT, Zhou XY, Vasyliunas VM, Haerendel G, Arballo JK, et al. 2001. Interplanetary Shocks, Magnetopause Boundary Layers and Dayside Auroras: The Importance of a Very Small Magnetospheric Region. *Surv. Geophys.* **22**: 101–130. https://doi.org/10.1023/A:1012952414384.

Tsurutani, BT, Gonzalez WD, Gonzalez ALC, Guarnieri FL, Gopalswamy N, et al. 2006a. Corotating solar wind streams and recurrent geomagnetic activity: A review. *J. Geophys. Res.* **111**: A07S01. https://doi.org/10.1029/2005JA011273.

Tsurutani, BT, McPherron RL, Gonzalez WD, Lu G, Gopalswamy N, et al. 2006b. Magnetic storms caused by corotating solar wind streams. In BT Tsurutani, R McPherron, W Gonzalez, G Lu, JHA Sobral, N Gopalswamy (Eds.), *Geophys Mono Ser* (Vol. **167**, pp. 1–17). Washington, D.C.: Am Geophys Union. https://doi.org/10.1029/167GM03.

Tsurutani, BT, Echer E, Gonzalez WD. 2011. The solar and interplanetary causes of the recent minimum in geomagnetic activity (MGA23): a combination of midlatitude small coronal holes, low IMF B_Z variances, low solar wind speeds and low solar magnetic fields. *Ann. Geophys.* **29**, 839–849. https://doi.org/10.5194/angeo-29-839-2011.

Tsurutani, BT, Lakhina GS, Verkhoglyadova OP, Gonzalez WD, Echer E, et al. 2011b. A review of interplanetary discontinuities and their geomagnetic effects. *J Atmos Sol Terr Phys* **73**: 5–19. https://doi.org/10.1016/j.jastp.2010.04.001.

Tsurutani, BT, Hajra R, Echer E, Gonzalez WD, Santolik O. 2016, June 1. *Predicting Magnetospheric Relativistic >1 MeV Electrons (Version 40)*. Retrieved from http://www.techbriefs.com/component/content/article/ntb/tech-briefs/software/24815.

Tsurutani, BT, Hajra R, Lakhina GS, Meng X. 2024. Revisiting the superstorm on 6–7 April 2000 caused by an extraordinary corotating interaction region (With an Embedded Coronal Jet?). *J. Geophys. Res. Space Physics* **129**: e2024JA032989. https://doi.org/10.1029/2024JA032989.

Wang, H, Lühr H. 2023. Magnetic longitudinal and local time variations of polar electrojet and field-aligned currents. *J. Geophys. Res. Space Physics* **128**: e2023JA031874. https://doi.org/10.1029/2023JA031874.

Wang, H, Lühr H, Ma SY. 2005. Solar zenith angle and merging electric field control of field-aligned currents: A statistical study of the Southern Hemisphere. *J. Geophys. Res. Space Physics* **110**: 2004JA010530. https://doi.org/10.1029/2004JA010530.

Wang, H, Lühr H, Ma SY, Weygand J, Skoug RM, et al. 2006. Field-aligned currents observed by CHAMP during the intense 2003 geomagnetic storm events. *Ann. Geophys.* **24**: 311–324. https://doi.org/10.5194/angeo-24-311-2006.

Wang, H, Cheng Q, Lühr H, Zhong Y, Zhang K, et al. 2024. Local time and hemispheric asymmetries of field-aligned currents and polar electrojet during May 2024 superstorm periods. *J. Geophys. Res. Space Physics* **129**: e2024JA033020. https://doi.org/10.1029/2024JA033020.

Waters, CL, Anderson BJ, Liou K. 2001. Estimation of global field aligned currents using the iridium® System magnetometer data. *Geophys. Res. Lett.* **28**: 2165–2168. https://doi.org/10.1029/2000GL012725.

Wilder, FD, Crowley G, Anderson BJ, Richmond AD. 2012. Intense dayside Joule heating during the 5 April 2010 geomagnetic storm recovery phase observed by AMIE and AMPERE. *J. Geophys. Res. Space Physics* **117**: 2011JA017262. https://doi.org/10.1029/2011JA017262.

Zhong, Y, Wang H, Zhang K, Xia H, Qian C. 2022. Local time response of auroral electrojet during magnetically disturbed periods: DMSP and CHAMP coordinated observations. *J. Geophys. Res. Space Physics* **127**: e2022JA030624. https://doi.org/10.1029/2022JA030624.

Zirker, JB. 1977. Coronal holes and high-speed wind streams. *Rev. Geophys.* **15**: 257–269. https://doi.org/10.1029/RG015i003p00257.

Cite this article as: Hajra R, Tsurutani BT, Franco AMS, Lu Q, Du A, et al.2026. Field-aligned currents are strongly modulated by corotating solar wind high-speed streams. *J. Space Weather Space Clim*. **16**, 18. https://doi.org/10.1051/swsc/2026007

Appendix A: List of HSSs

Table A1. HSSs under this study. Sunward (anti-sunward) HSSs are emanated from solar coronal holes with negative (positive) magnetic polarity, and are characterized by positive (negative) IMF B_x and negative (positive) B_y components.

HSS V_p peak (km s^{-1})	V_p peak time (UT)	HSS polarity
675	05 Jun 2016 22:39	Sunward
728	15 Jun 2016 07:59	Anti-sunward
564	24 Jun 2016 15:24	Sunward
486	03 Jul 2016 04:52	Sunward
670	09 Jul 2016 15:17	Anti-sunward
729	15 Jul 2016 03:17	Anti-sunward
646	29 Jul 2016 09:27	Sunward
713	05 Aug 2016 20:03	Anti-sunward
673	10 Aug 2016 09:22	Anti-sunward
607	24 Aug 2016 03:40	Sunward
748	03 Sep 2016 19:14	Anti-sunward
774	20 Sep 2016 11:50	Sunward
758	29 Sep 2016 06:35	Anti-sunward
781	17 Oct 2016 19:14	Sunward
793	25 Oct 2016 17:32	Anti-sunward
775	12 Nov 2016 18:58	Sunward
731	25 Nov 2016 20:03	Anti-sunward
761	10 Dec 2016 06:27	Sunward
784	23 Dec 2016 22:23	Anti-sunward
582	31 Dec 2016 20:55	Anti-sunward
773	06 Jan 2017 02:21	Sunward
648	19 Jan 2017 02:06	Anti-sunward
662	27 Jan 2017 10:50	Anti-sunward
790	31 Jan 2017 18:15	Sunward
612	19 Feb 2017 01:07	Anti-sunward
673	24 Feb 2017 05:39	Anti-sunward
760	03 Mar 2017 11:48	Sunward
719	22 Mar 2017 10:56	Anti-sunward
752	28 Mar 2017 04:25	Sunward
649	08 Apr 2017 16:16	Sunward
818	23 Apr 2017 20:57	Sunward
635	16 May 2017 06:06	Anti-sunward
764	20 May 2017 12:47	Sunward

Appendix B: ICMEs

Figure B1 shows an ICME and associated FAC variations during 19–23 July 2016. Sharp and simultaneous increases in the solar wind V_p (Fig. B1a), N_p (Fig. B1b), P_{sw} (Fig. B1b), T_p (Fig. B1c), and IMF B_0 (Fig. B1d) at ~23:52 UT on 19 July represent a fast forward (FF) interplanetary shock (Kennel et al., 1985; Tsurutani et al., 2011b) (marked by a vertical dashed line, detail shock analysis is beyond scope of the present work) that caused a sudden impulse (SI$^+$; Araki et al., 1993; Tsurutani et al., 2011b; Tsurutani & Lakhina, 2014) of +55 nT in SYM-H (Fig. B1f). The shock is caused by the interplanetary counterpart of a fast coronal mass ejection (CME), which was erupted from a solar active region at ~18:00 UT on 18 July. The shock compressed the plasma and IMF up to ~13:14 UT on 20 July, resulting in an interplanetary sheath (Kennel et al., 1985; Tsurutani et al., 1988). The sheath is followed by a region up to ~14:58 UT on 22 July (marked by a gray shading), where IMF components exhibit smooth rotations in polarities, T_p, and plasma-β (β being the ratio of the plasma pressure to the magnetic pressure) are low. This is called a magnetic cloud (MC; Burlaga et al., 1981; Gonzalez & Tsurutani, 1987; Marubashi & Lepping, 2007). While B_z had some small southward components in the sheath, it was weak, and the IMF was mainly northward during the MC. The shock triggered significant flux opening (high N_{CF}) at the dayside magnetopause (Fig. B1e) during the sheath. As a consequence, there is some moderate substorm activity (Fig. B1g) and FAC enhancements (Fig. B1h) during the sheath. However, the MC is characterized by extremely low values of N_{CF} and Φ_D, no significant substorm activity, and no FAC enhancements.

The 12–20 October 2016 interval, shown in Figure B2, is characterized by an ICME followed by a solar wind HSS. The FF shock at ~22:12 UT on 12 October, marked by sharp increases in V_p (Fig. B2a), N_p (Fig. B2b), P_{sw} (Fig. B2b), T_p (Fig. B2c), and IMF B_0 (Fig. B2d), is caused by the interplanetary counterpart of a fast CME erupted from the Sun at ~19:24 UT on 11 October. The shock led to an SI$^+$ of +20 nT (Fig. B2f), followed by an interplanetary sheath of compressed plasma and fluctuating IMF up to ~06:09 UT on 13 October. The sheath is followed by an MC up to ~16:53 UT on 14 October (marked by a gray shading). It is characterized by a strong IMF B_0, with clear and smooth rotations in its components, low T_p, and β. The strong IMF southward component B_z = –21 nT is associated with prominent increases in N_{CF} (Fig. B2e), Φ_D (Fig. B2e), strong substorm activity with peak SML = –2292 nT (Fig. B2g), an intense storm with SYM-H peak = –114 nT (Fig. B2f), and prominent FAC intensifications up to ~11 MA (Fig. B2h).

The MC is followed by a gradual rise in V_p to a peak value of ~750–777 km s^{-1} during 16–18 October, and then a slow decay in V_p (Fig. B2a). This is identified to be an HSS emanated from a negative polarity coronal hole on 14 October (not shown). The entire HSS proper was characterized by enhanced FACs of ~6 MA (Fig. B2h).

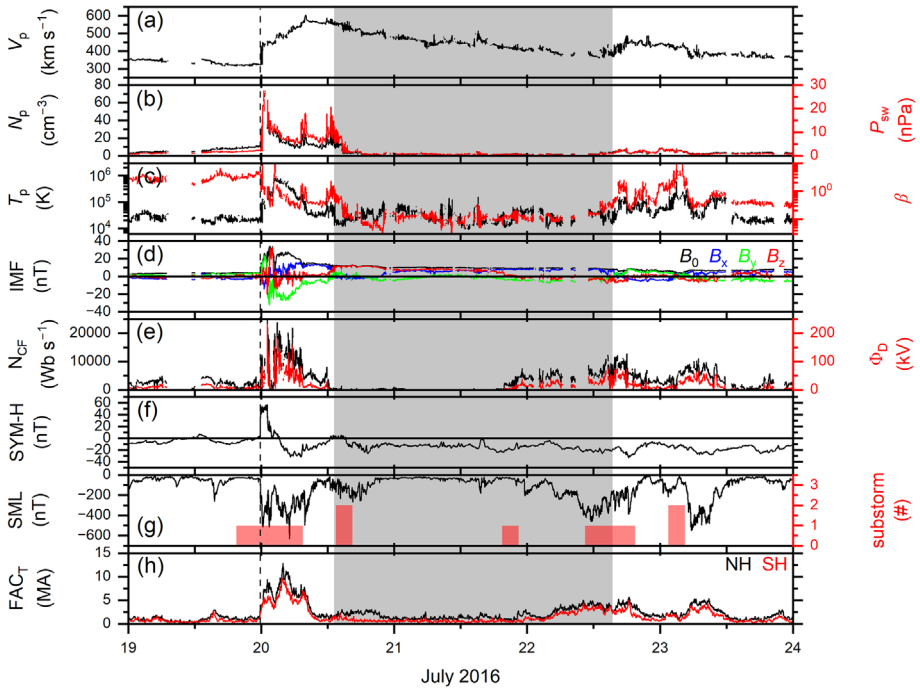

Figure B1. Solar wind, geomagnetic conditions, and FACs associated with an ICME during 19–23 July 2016. From top to bottom, the panels are: (a) solar wind V_p, (b) N_p (black, legend on the left) and P_{sw} (red, legend on the right), (c) T_p (black, legend on the left) and plasma-β (red, legend on the right), (d) IMF B_0, and B_x, B_y, and B_z components, (e) N_{CF} (black, legend on the left) and Φ_D (red, legend on the right), (f) SYM-H index, (g) SML index (black, legend on the left) and substorm numbers in each 3-h interval (red, legend on the right), and (h) FAC_T in the northern hemisphere (NH; black) and southern hemisphere (SH; red). The dashed vertical line indicates an FF shock, and the shaded region is an MC.

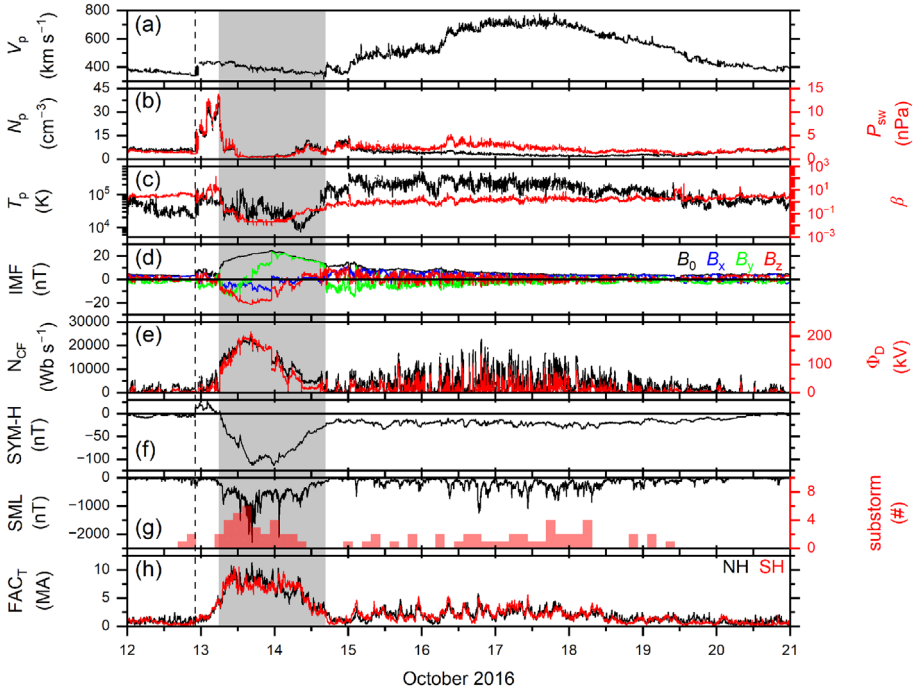

Figure B2. Solar wind, geomagnetic conditions, and FACs associated with an ICME followed by an HSS during 12–20 October 2016. Panels are the same as in Figure B1. The dashed vertical line indicates an FF shock, and the shaded region is an MC.

Appendix C: Periodograms and wavelet coherence

Figure C1 shows Lomb-Scargle periodogram analyses of solar wind plasma, IMF, coupling functions, geomagnetic indices, and FAC intensities. Separate analyses are done for currents in the northern and southern hemispheres, and for dayside and nightside FACs.

The V_p periodogram is characterized by two prominent peaks: the strongest one at ~26 days, and a slightly weaker peak (~74% of the strongest peak) at ~13.6 days (Fig. C1a). For the plasma parameters N_p, $P_{sw,}$ and T_p, the ~26 and 13.6-day periodicities have comparable amplitudes (Fig. C1b). In addition, T_p exhibits a prominent peak (~59%) at ~29 days, while P_{sw} exhibits shorter periods of ~6.8 (~86%), ~4.5 (~71%), ~6.6 (~56%), 8.7 (~54%), and ~4.4 (~50%) days (in descending order of amplitude). IMF B_0 exhibits the strongest peak at ~13.6 days, while B_z at ~25.3 days, with secondary peaks at ~14.1 (~87%) and multiple shorter (~2.7, 3.5, 2.5, 6.3, 4.2, 3.9 days) and longer (~25.4, 36.1, 29.3 days) periodicities (Fig. C1c).

Φ_D and N_{CF} are characterized by the strongest peak at ~13.8 days, followed by two peaks at ~26.1 (62–89%) and ~29.2 (68–76%) days (Fig. C1d). The Φ_D and N_{CF} periodicities are also present in the SML index (Fig. C1e), as well as in the FAC intensities (Fig. C1f–C1h). The strongest peak in FACs is noted at ~13.8 days, followed by peaks at ~26.2 and ~29.2 days. The periodicities are more or less the same for dayside, nightside, and total FACs in both the northern and southern hemispheres.

Figure C2 shows the wavelet coherences between the northern hemispheric total FAC intensity and V_p (Fig. C2a), and between FAC intensity and N_{CF} (Fig. C2b), with the arrows representing the phase differences (as in Fig. 4). FAC intensity is strongly coherent to N_{CF} for most of the periods. However, FAC exhibits lesser coherence with V_p for periods < 7 days, periods of ~18–20 days, and periods of ~39–56 days. In other words, FAC intensity is much more coherent to N_{CF} than to V_p.

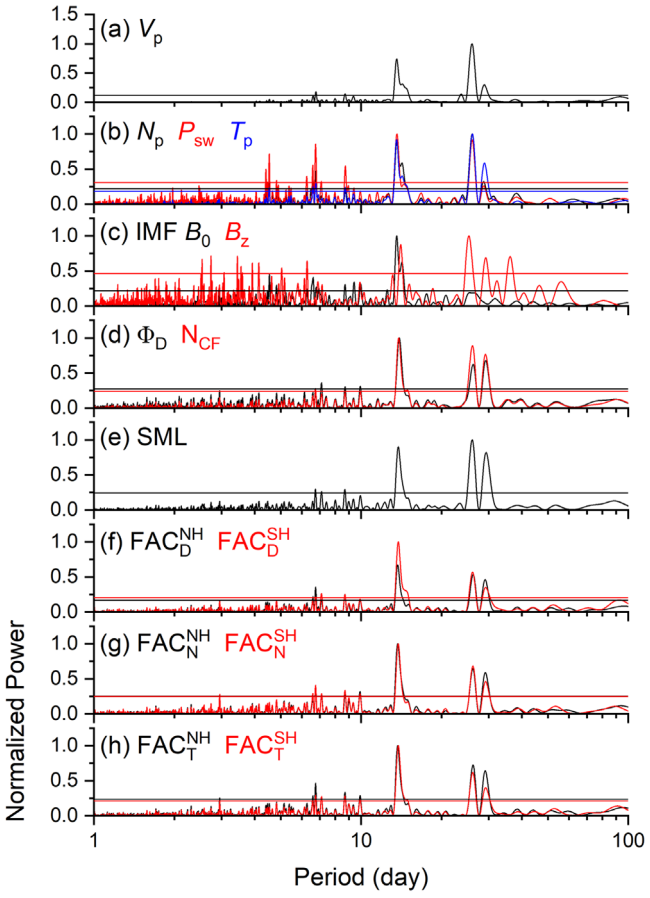

Figure C1. Lomb-Scargle periodograms of solar wind plasma and IMF parameters, solar wind-magnetosphere coupling functions, auroral electrojet indices, and FAC intensities. In panels (f)–(h), T represents total, D is dayside, N is nightside, NH is the northern hemisphere, and SH is the southern hemisphere. Horizontal lines in each panel indicate 95% confidence levels of the periodograms. For the periodogram analyses, we used the highest resolution data available, i.e., 2 min for FACs and 1 min for all other parameters.

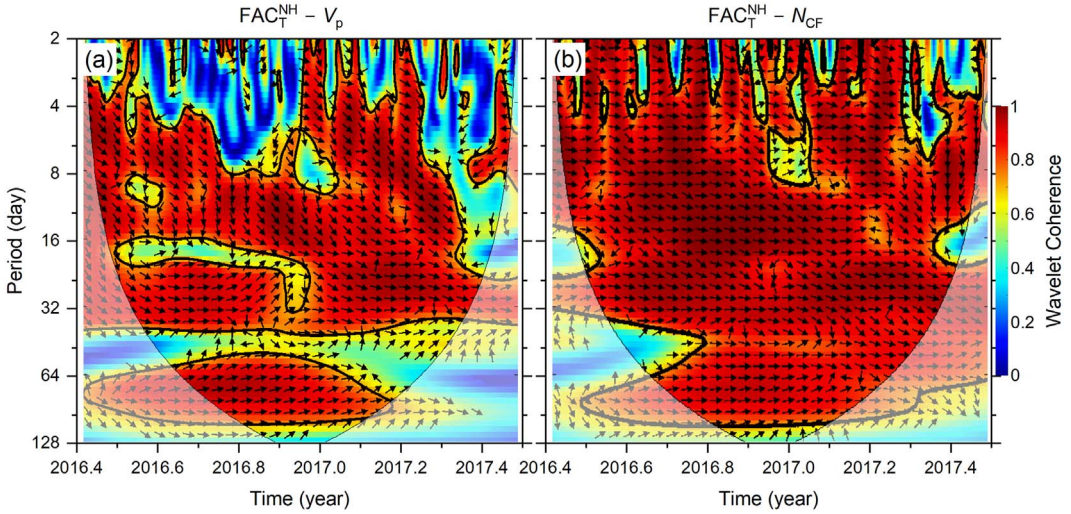

Figure C2. Wavelet coherence (a) between northern hemispheric total FAC intensity and V_p, and (b) between northern hemispheric total FAC intensity and N_{CF}. Wavelet coherence values are shown by the color bar at the right. The cone of influence, where edge effects might distort the results, is shown as lighter shades. The relative phase relationships (of FAC intensity with V_p and N_{CF}) are shown as arrows, horizontal right arrows indicating in-phase, horizontal left arrows indicating anti-phase. All data are processed into 30 min resolution so that they precisely coincide (in time) with each other.